

Effect of Hot-Rolling on Microstructures and Mechanical Properties of Extruded Mg-6Gd-3.2Y-xZn-0.5Zr Sheet

Liang Zheng, Chuming Liu, Jing Jin, Xiao Wang, and Dawei Ji

(Submitted August 18, 2011; in revised form February 14, 2012; published online May 1, 2012)

The optical microscope (OM), scanning electron microscope (SEM), high-resolution transmission electron microscope (HRTEM), x-ray diffractometer (XRD), x-ray energy spectrometer, Vickers hardness tester, and universal tensile test machine were employed to investigate the effects of Zn additions and hot-rolling on microstructures, aging behaviors, and mechanical properties of Mg-6Gd-3.2Y-0.5Zr extruded sheet. Block-shaped and acicular LPSO structures are found in the alloy containing Zn. The block-shaped LPSO structures can refine the microstructure and improve the secondary deforming ability. The size of β' phases between the acicular LPSO structures decreases greatly. Both the block-shaped and acicular LPSO structures can improve the tensile mechanical properties of the Mg-Gd-Y-Zn-Zr alloys. Secondary deformation which gives rise to residual stress can promote age-hardening behavior and shrinks the peak-aging time. Owing to LPSO structures and the secondary deformation, T10 sample of alloy C obtains the highest proof strength of 375 MPa and tensile strength of 420 MPa.

Keywords aging behavior, mechanical properties, Mg-6Gd-3.2Y-0.5Zr alloy, microstructures, secondary deformation

1. Introduction

Magnesium alloys containing rare earth metals have received a tremendous amount of attention owing to their low density, and high specific strength at room and elevated temperatures (Ref 1-5). However, their application has been limited because of the inferior absolute mechanical properties. Alloying and plastic deformation are effective approaches to improve the strength and ductility simultaneously because of the refinement of the microstructures through dynamic recrystallization (DRX). Previous researchers have done many studies regarding these two aspects. Gd, Y, and Zn are the common additive elements in magnesium alloys. Peng et al. (Ref 6) reported that Y addition could refine the microstructures of Mg-7Gd alloy and enhance the ageing-hardening behavior because the precipitations increase. As is well known, β'' phase with DO_{19} structure and β' phase with base-centered orthorhombic (bco) structure both have aging-strengthening effect in Mg-Gd-RE alloys (RE represents Y and Nd). β'' phase is the main strengthening contributor in the initial stage of aging, which turns into β' phase with holding time. At peak-aged stage, β' phase should be considered as the main strengthening contributor (Ref 7-9).

Nie (Ref 10) reported that Zn addition could improve the tensile mechanical properties of Mg-6Gd-0.6Zr alloy. Mg-5Gd alloy with Zn (1 wt.%) shows an obvious aging-strengthening behavior (Ref 11). 18R-type long-period stacking order (LPSO)

structure found in the as-cast Mg-Zn-Y alloy transforms to the 14H-type LPSO structure by annealing at 773 K (Ref 12). Hot-extruded Mg-2.3Zn-14Gd (wt.%) can precipitate 14H-type LPSO structure during aging at 623 K, and this kind of LPSO structure can improve the alloy's proof strength and elongation (Ref 13). Honma et al. (Ref 14) found that Zn addition could minimize the total energy in the systems and improve the elongation by promoting the precipitation of β_1 and LPSO structure. Hou et al. (Ref 15) developed the extruded Mg-6.5Gd-1.3Nd-0.7Y-0.3Zn sheet, room-temperature tensile strength and elongation of which reach 310 MPa and 5.8%, respectively, after aging at 473 K.

However, the previous investigations on plastic deformation of magnesium alloys were limited to one-deformation technique. The investigation on combining different deformation techniques has never been reported. In this article, the effects of Zn addition and hot rolling on the microstructures, aging-strengthening behaviors and tensile mechanical properties of extruded Mg-6Gd-3.2Y-0.5Zr sheet are investigated.

2. Experimental Procedures

The chemical compositions of the designed alloys are listed in Table 1. The alloys' ingots were prepared in an electric resistance furnace. The melting was conducted at about 1023-1053 K, covered with anti-oxidizing gas $CO_2:SF_6 = 99:1$. At about 1003 K, the melt was poured into steel mold with an ingot diameter of 65 mm. The chemical compositions of the alloys were determined by inductively coupled plasma atomic emission spectrum (ICP-AES) apparatus. The cylindrical ingots were homogenized at 773 K (A: for 4 h; B-D: for 30 h) in a muffle furnace followed by quenching into hot water. The homogenized ingots were machined into cylindrical ingots with a diameter of 60 mm, and then extruded into sheets with the size of 40×5.8 mm at 723 K. Some of the extruded sheets were rolled to sheets with the thickness of 4.6 mm at 773 K for

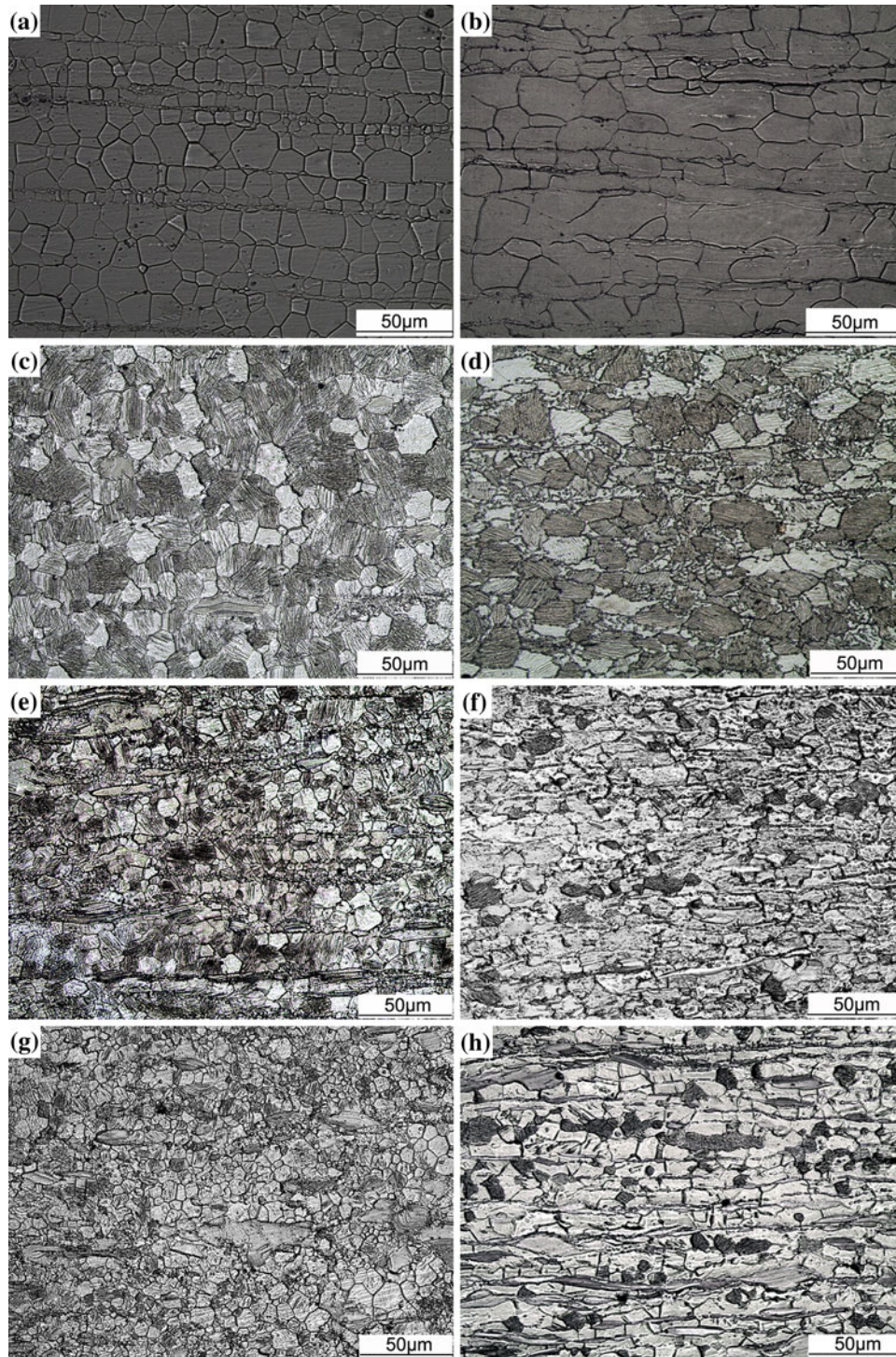
Liang Zheng, Chuming Liu, Jing Jin, Xiao Wang, and Dawei Ji, School of Materials Science and Engineering, Central South University, Changsha 410083, China. Contact e-mail: zhengl2010@yahoo.com.cn.

Table 1 Chemical composition of the alloys

	Gd, wt. %	Y, wt. %	Zn, wt. %	Zr, wt. %	Mg, wt. %
A	6.2	3.1	0.0	0.5	Bal
B	6.0	3.3	0.7	0.4	Bal
C	5.9	3.4	1.4	0.4	Bal
D	6.1	3.4	2.3	0.5	Bal

two passes, with the reduction rate of 21%. The rolling direction was parallel to the extrusion direction. Some of the extruded and extruded-rolled sheets were directly aged at 473 K to investigate the age-hardening behavior.

Tensile tests were carried out using a universal tensile testing machine at a speed of 2 mm/min with the load axis parallel to the deformation direction. Vickers hardness was measured using a HVS-1000 hardness tester with a load of 4.9 N and a dwelling time of 15 s. The microstructures of the alloys were observed

**Fig. 1** OM images of the alloys in different conditions: (a, b) alloy A, (c, d) alloy B, (e, f) alloy C, and (g, h) alloy D

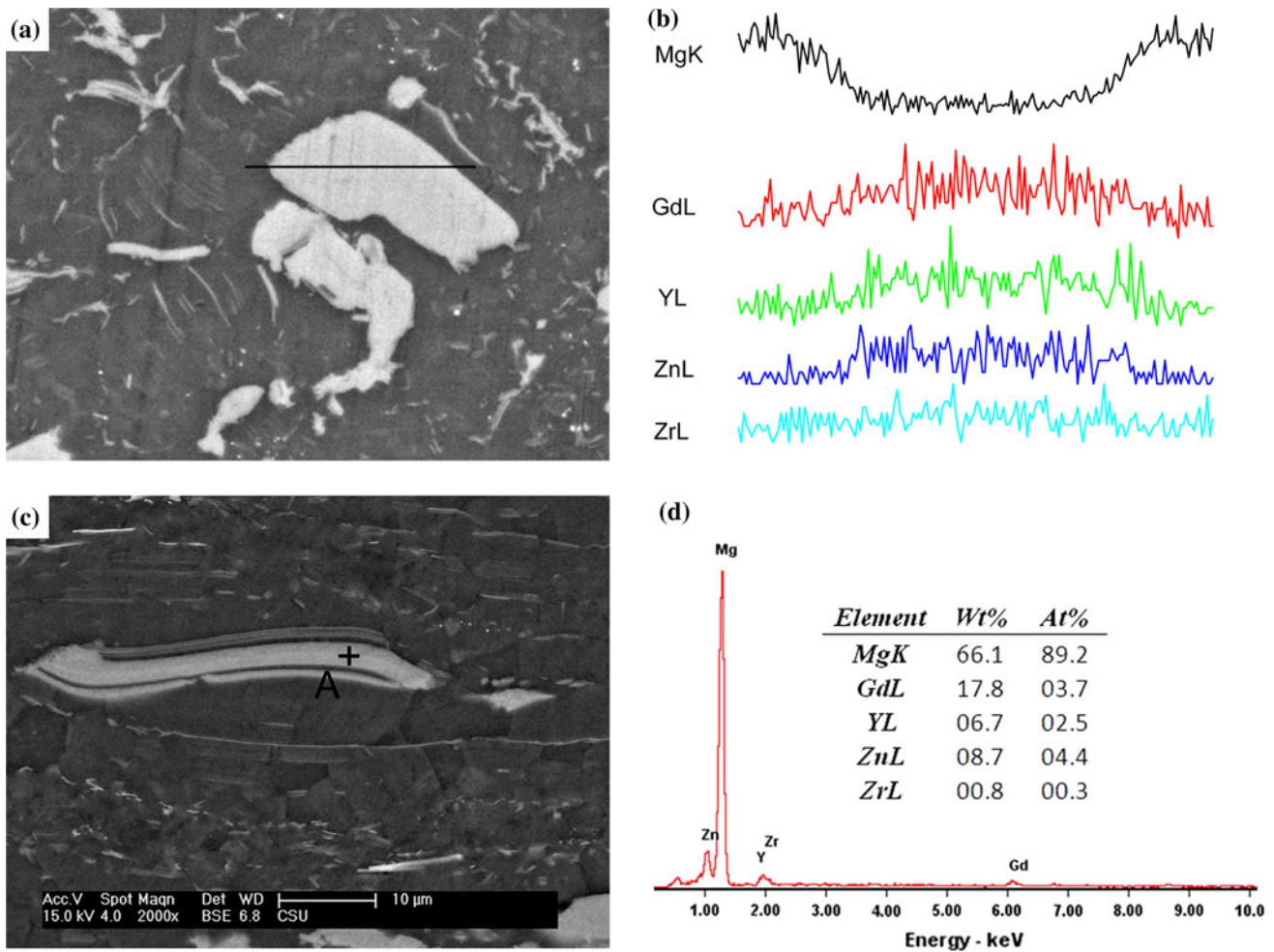


Fig. 2 (a) Transverse direction SEM image of the as-extruded sample D, (b) the result of linear SEM-EDS, (c) longitudinal direction SEM image of the extruded sample D, and (d) EDS result of point A

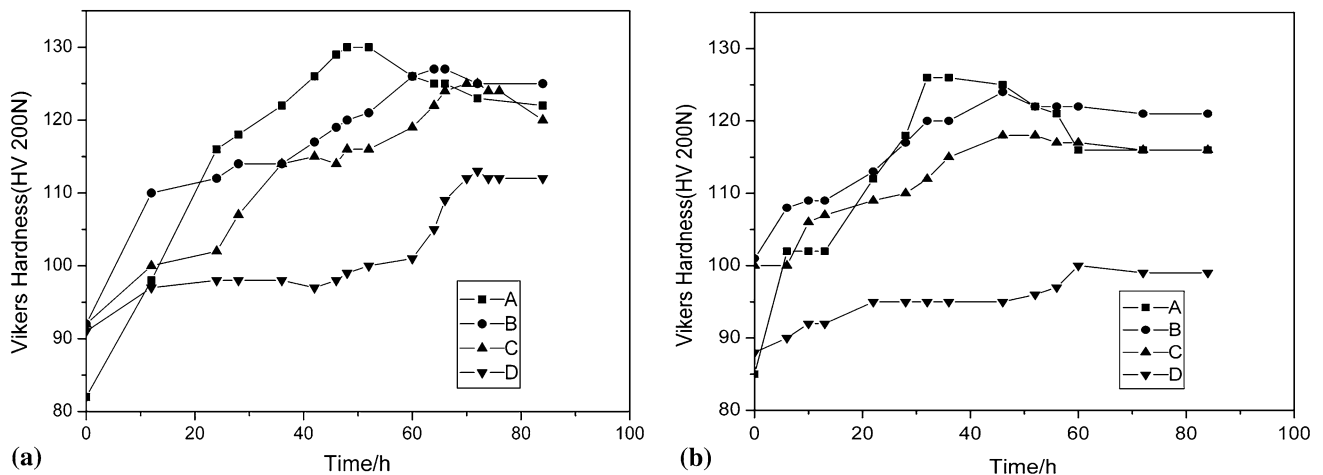


Fig. 3 Aging hardening curves. (a) Extruded samples and (b) extruded-rolled samples

using a Leica optical microscope (OM) and Sirion200 field emission scanning electron microscope (SEM) at 15 kV. Samples for metallography were etched in a solution of 6 g picric acid, 40 mL acetic acid, 40 mL water, and 100 mL ethanol. Transmission electron microscope (TEM) and high resolution transmission electron microscope (HRTEM) observation were

performed using a JEM 2100F HRTEM operated at 200 kV. Specimens for TEM were prepared with an argon ion milling technique. Phase analysis was conducted using D/Max2500 x-ray diffractometer (XRD) at 36 kV—the scanning speed is 2°min^{-1} —and GENESIS-60S energy dispersive spectroscope (EDS).

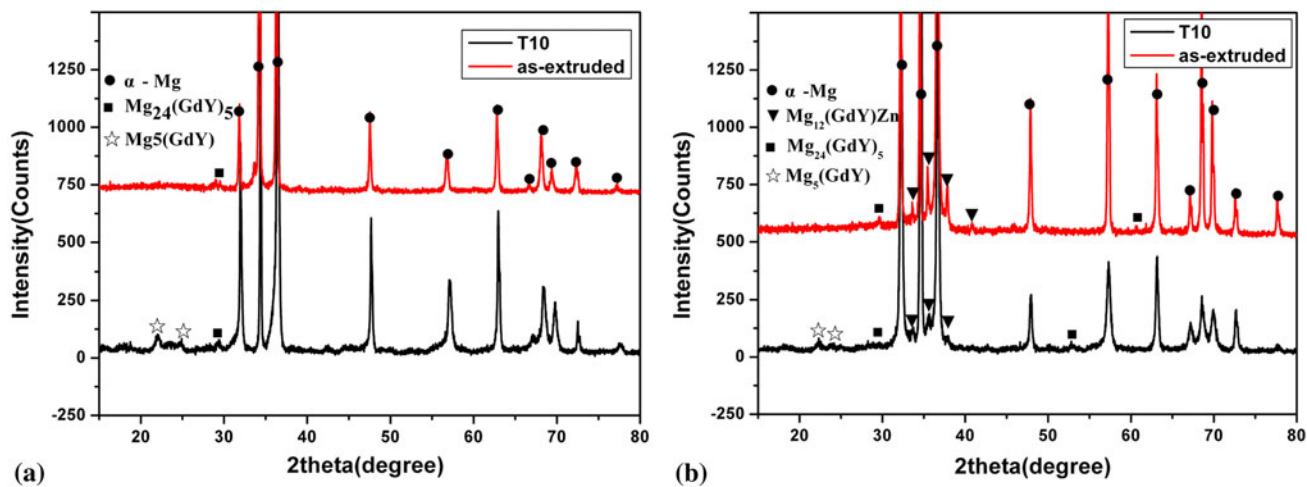


Fig. 4 XRD results of the extruded and aged Sample. (a) Alloy A and (b) alloy C

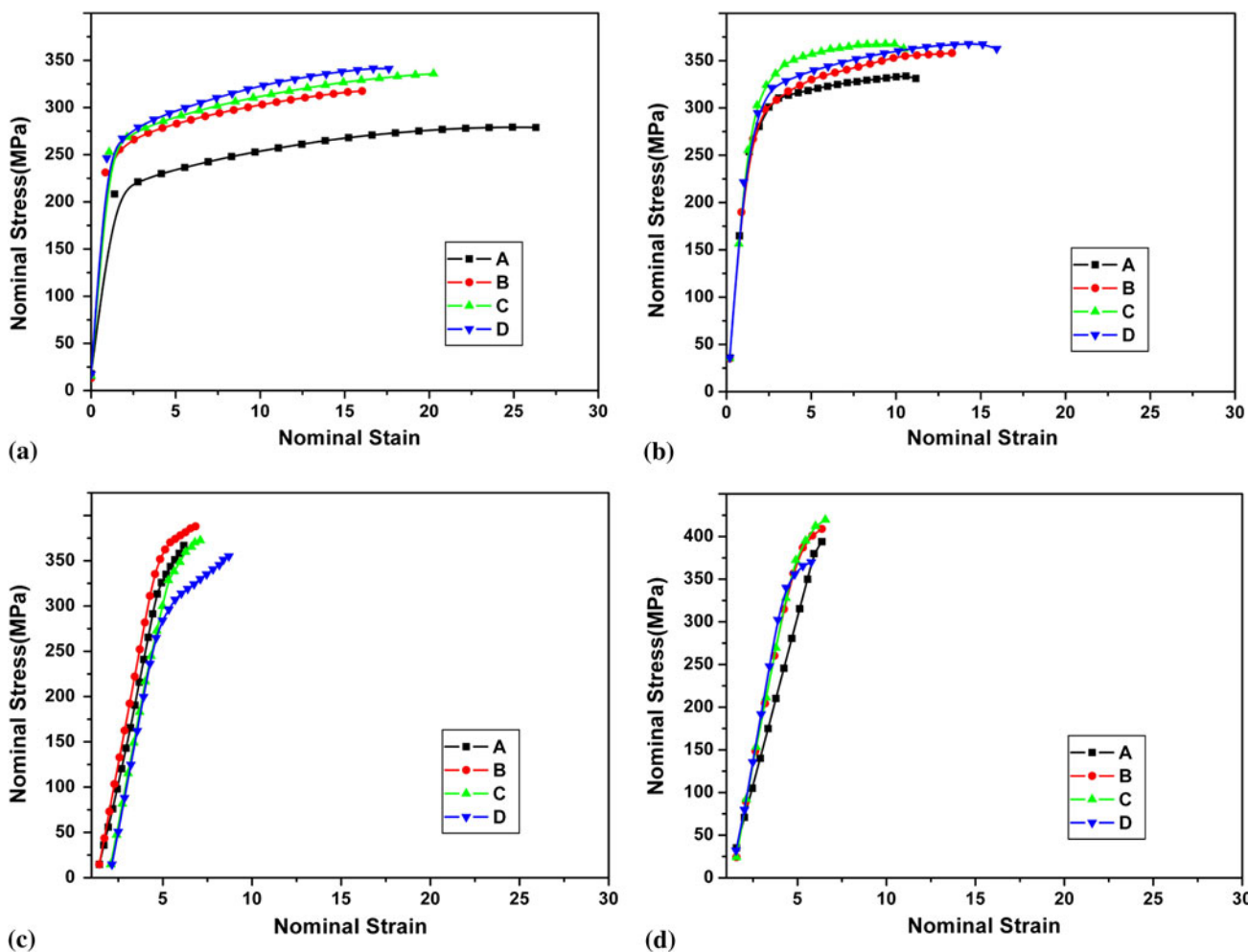
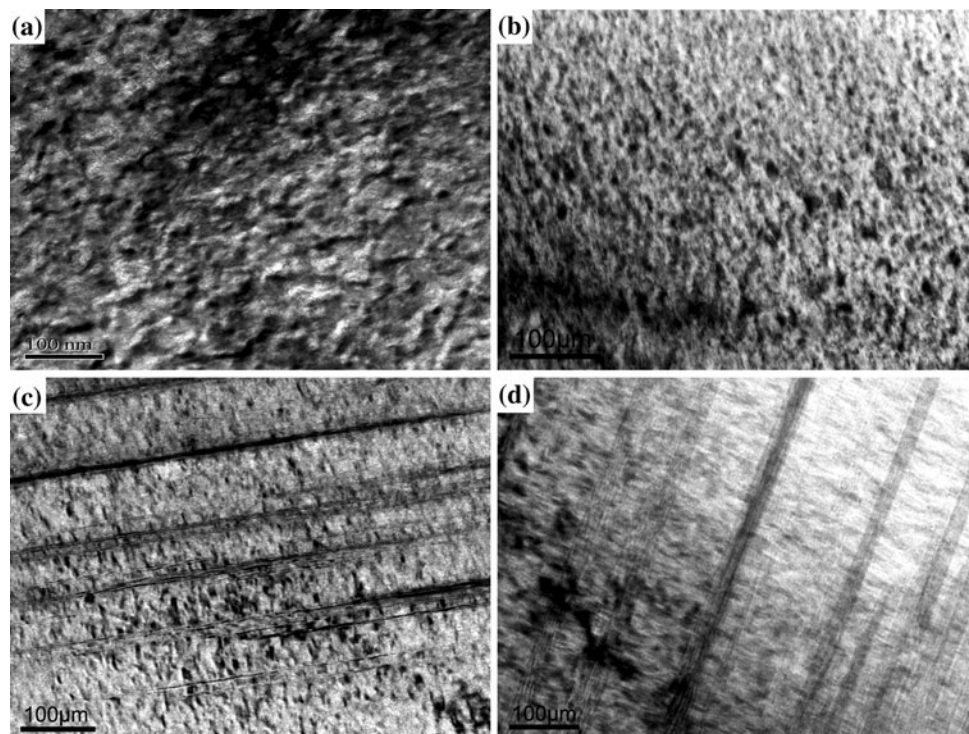


Fig. 5 Nominal stress-stain curves of the alloys in different conditions. (a) Extruded samples, (b) extruded-rolled samples, (c) T5 samples, and (d) T10 samples

Table 2 Tensile mechanical properties of the alloys in different conditions

	Extruded			Extruded + rolled			T5			T10		
	$\sigma_{0.2}$, MPa	σ_b , MPa	δ , %	$\sigma_{0.2}$, MPa	σ_b , MPa	δ , %	$\sigma_{0.2}$, MPa	σ_b , MPa	δ , %	$\sigma_{0.2}$, MPa	σ_b , MPa	δ , %
A	180	280	19	260	330	9	292	369	5.3	348	375	5
B	210	318	11	262	358	10	365	389	6	369	410	5.2
C	228	336	15	280	368	8	323	372	6.5	375	420	5.6
D	233	343	14	275	372	12	280	355	7.3	346	370	7

**Fig. 6** (a) BF image of sample A in T5 condition, (b) BF image of sample A in T10 condition, (c) BF image of sample C in T5 condition, and (d) BF image of sample C in T10 condition

3. Results and Discussion

Figure 1 shows the OM images of the longitudinal section of the extruded and extruded-rolled samples. As for the extruded samples, the equiaxed grains indicate that DRX occurred in the four alloys during extrusion. The grain size decreases with the increase of Zn content. When Zn content reaches 1.4 wt.%, the grain size does not decrease any more. LPSO structures are found in the alloys containing Zn, image and distribution of which vary much with the content of Zn. The LPSO structures in Alloy B (0.7 wt.% Zn) are needle-like and distribute in the interior of the grains. The majority of the LPSO structures in alloy C and alloy D are block-like and distribute at grain boundaries. As for the extruded-rolled samples, the grains are extended along rolling direction. Owing to the high rolling temperature, the grain size of the extruded-rolled alloy A increased obviously compared with the extruded sample, while the grain growth cannot be clearly observed in alloy B-D. It can be concluded that the LPSO structures can inhibit the grain growth. Moreover, the block-like LPSO structures at grain boundaries can block grain boundary

migration, which manifests that the block-like LPSO structures play a more important role of inhibiting the grain growth than the needle-like ones.

Figure 2 shows the SEM images and the corresponding EDS results of the extruded D alloy. The white LPSO structures can be seen clearly. The needle-like and block-like LPSO structures are both extended along the extrusion direction (Fig. 2c). The result of linear SEM-EDS in Fig. 2(b) suggests that the LPSO structures are enriched in Gd, Y, and Zn. The composition of the LPSO structure is Mg-6.2at.% RE-4.4at.% Zn according to the EDS result (Fig. 2d), and this is consistent with the results of Itoi (Ref 12).

Figure 3 gives the aging-hardening curves of the extruded and extruded-rolled samples. All the four alloys exhibit obvious age hardening response. The Vickers hardness values of extruded and extruded-rolled alloy B, C and D are higher than that of the Zn-free alloy A, which suggests better tensile mechanical properties. With the increase of Zn addition, however, the aging-hardening rates and peak hardness decrease. Compared with the extruded samples, the peak-aging times of the extruded-rolled samples decreased obviously. This can be

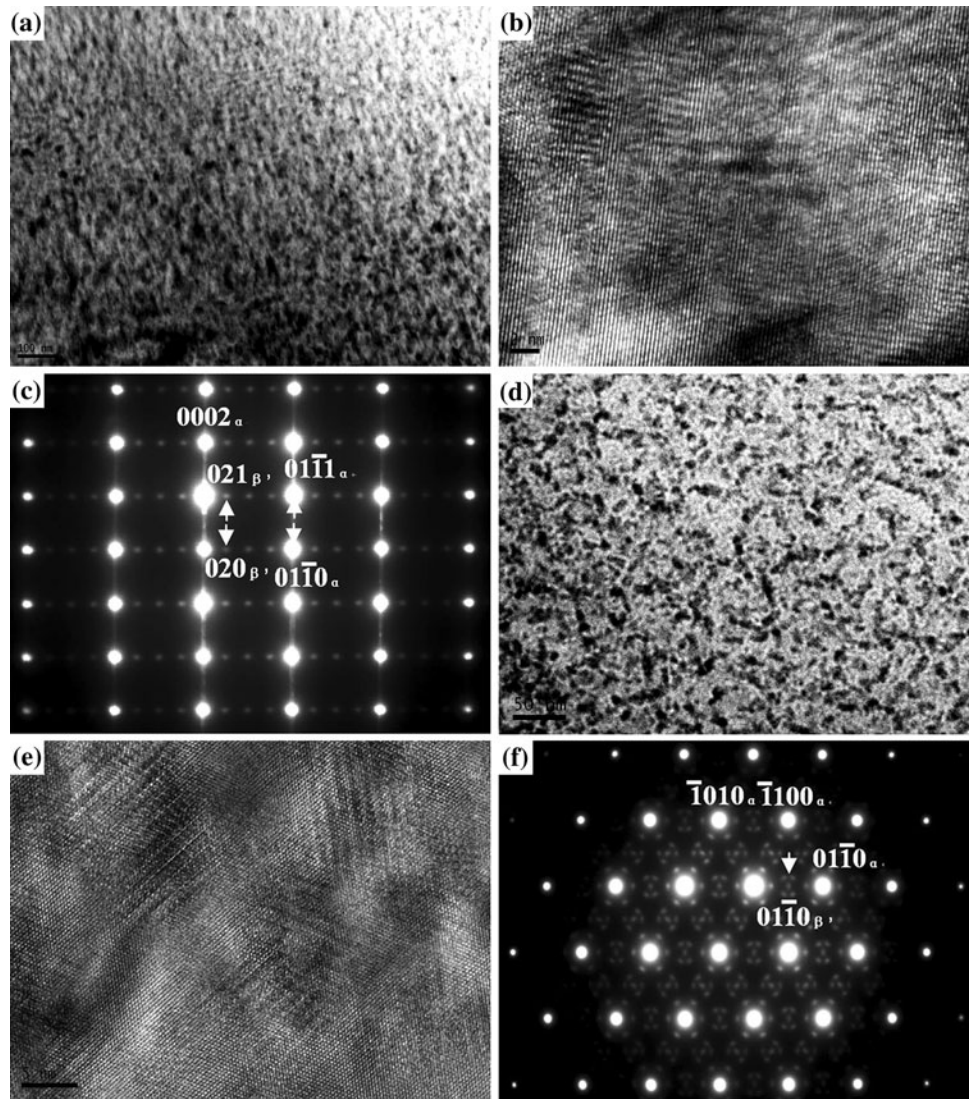


Fig. 7 (a) TEM BF image of β' phases of the $[2\bar{1}\bar{1}0]$ zone axis, (b) HRTEM image of β' phases of the $[2\bar{1}\bar{1}0]$ zone axis, (c) The corresponding SAED pattern ($B//[2\bar{1}\bar{1}0]$), (d) TEM BF image of β' phases of the $[0001]$ zone axis, (e) HRTEM image of β' phases of the $[0001]$ zone axis, and (f) The corresponding SAED pattern ($B//[0001]$)

explained by the residual stress generated by hot rolling. The residual stress can promote the diffusion process during aging, which accelerates the precipitation of β' phase.

Figure 4 is the XRD results of alloy A (Fig. 4a) and alloy C (Fig. 4b). As for alloy A, two phases are identified in extruded sample: α -Mg and $Mg_{24}(GdY)_5$. As for alloy C, three phases are identified in extruded sample: α -Mg, $Mg_{24}(GdY)_5$ and $Mg_{12}Zn(YGd)$. $Mg_5(GdY)$ phase is the specific phase generated by aging, which should be considered as the main contributor of aging hardening. $Mg_{12}Zn(YGd)$ phase is the specific phase in the alloys containing Zn. According to the SEM images and EDS result, it can be concluded that the LPSO structure was $Mg_{12}Zn(YGd)$.

Figure 5 gives the tensile stress-strain curves of the alloys in different conditions. To the extruded alloys, both the proof strength and tensile strength increase with Zn addition, yet the elongation decreases. Owing to the work hardening generated by rolling, the strengths of extruded-rolled alloys are higher than those of the extruded alloys. Interestingly, almost no elongation decrease can be seen in the alloy B-D, while the

elongation of alloy A decreases much. The LPSO structures can improve the alloys' elongation by coordinating deformation, which suggests a good ability of secondary deformation. The extruded-aged (T5) alloys show higher strengths than the extruded alloys. The tensile strength of the T5 alloy B reaches 390 MPa, and it is much higher than that of the T5 alloy A, C, and D. The high strength can be attributed to the acicular LPSO structures which affect the decomposition of the supersaturated solid solution. The block-like LPSO structures in alloys C and D distribute at grain boundaries. Many RE atoms are consumed by LPSO structures which impair the strength. Fortunately, the elongations of the alloys are improved by the block-like LPSO structure. The tensile strengths of alloys B and C are more than 400 MPa. T10 alloys gain the highest proof strengths and tensile strengths. The tensile mechanical properties of the alloys in different conditions are shown in Table 2.

Figure 6 gives the TEM images of the alloys A and C in T5 and T10 conditions. As for the alloy A, β' phases in T10 sample are smaller than that in T5 sample, distribution in T10 sample of which is more dispersive. As for the alloy C, similar phenomenon

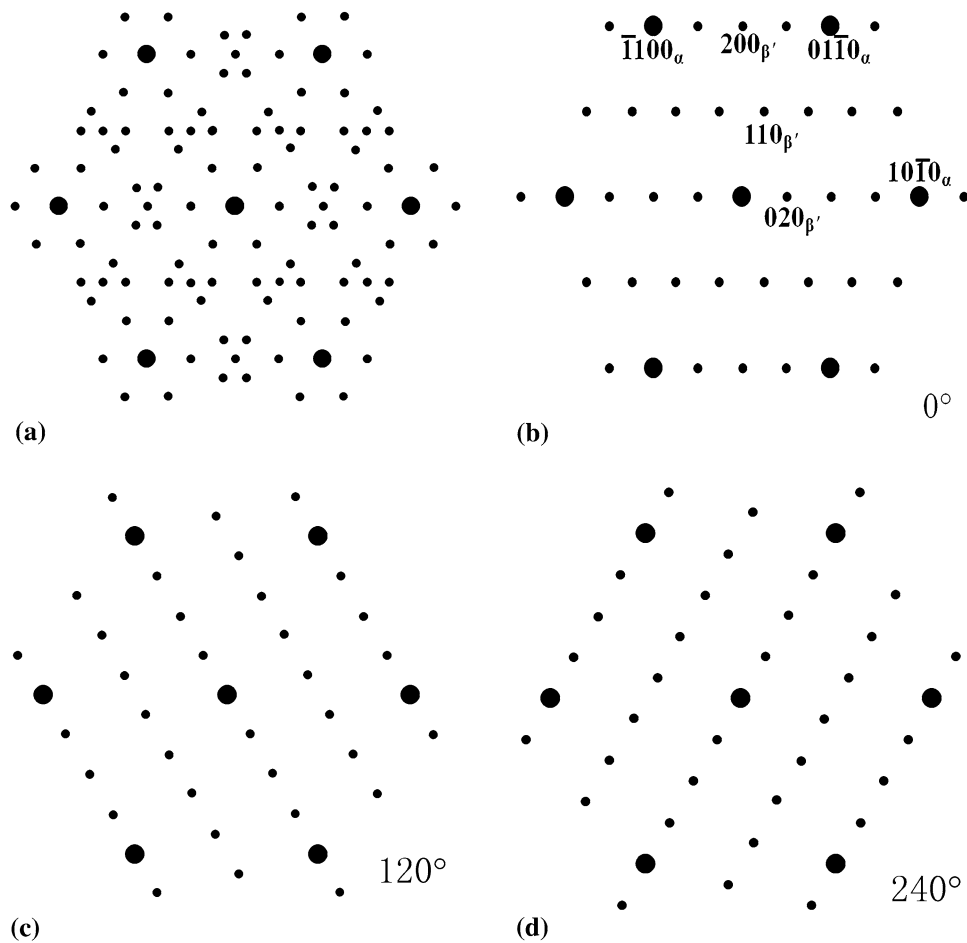


Fig. 8 (a) Schematic $[0001]_{\alpha}$ zone axis diffraction patterns for the β' phase and matrix; (b-d) $[0001]_{\alpha}$ SAED patterns of the three variants of the β' precipitates with an angle of 120° each other

can be observed in Fig. 6(c) and (d), which can produce the high proof strengths and tensile strengths of the T10 alloys. As depicted in Fig. 6(c) and (d), the β' phases distribute dispersively between two LPSO structures, which gives rise to the improvement of the tensile mechanical properties of the aged alloys containing Zn.

Figure 7 shows the TEM and HRTEM images of the β' phase of different zone axes. Figure 7(a) and (b) gives the BF and HRTEM images of the precipitation of the $[2\bar{1}\bar{1}0]$ zone axis, respectively. Figure 7(c) shows the corresponding selected area electron diffraction (SAED) pattern. The extra diffraction spots located at $1/4(01\bar{1}0)_{\alpha}$, $1/2(01\bar{1}0)_{\alpha}$ and $3/4(01\bar{1}0)_{\alpha}$. Figure 7(d) and (e) shows the TEM BF and the HRTEM images of the precipitation of the $[0001]$ zone axis, respectively. The extra diffraction spots at $1/2$ distance of $(1\bar{1}00)_{\alpha}$ or $(2\bar{1}\bar{1}0)_{\alpha}$ with the ones surrounding them. The $[0001]$ zone axis pattern is composed of three diffraction patterns of β' phases as depicted graphically in Fig. 8. It suggests that β' phase precipitates with three variants around the $[0001]$ zone axis. The angle of the three variants with each other is 120° , and it can be seen roughly in the TEM and HRTEM images of the $[0001]$ zone axis. Such a diffraction feature is typical in Mg-RE alloys containing a base-centered orthorhombic (bco) structure precipitation, with lattice parameters $a = 2 \times a_{\alpha\text{-Mg}} = 0.64$ nm,

$b = 8 \times d(10\bar{1}0)_{\alpha\text{-Mg}} = 2.22$ nm, $c = c_{\alpha\text{-Mg}} = 0.52$ nm (Ref 9, 14, 16). The orientation relationships between the β' phase and the $\alpha\text{-Mg}$ matrix are $(001)_{\beta'} // (0001)_{\alpha}$ and $[100]_{\beta'} // [2\bar{1}\bar{1}0]_{\alpha}$. According to the HRTEM images of the different zone axes, precipitate contrasts can be observed clearly (Fig. 7c and f).

The β' plates form on the $(01\bar{1}0)_{\alpha}$ or $(11\bar{2}0)_{\alpha}$ prismatic planes of $\alpha\text{-Mg}$, and the angle between the habit plane of the precipitate plates and $(0001)_{\alpha}$ slip plane is 90° . The cross section of the prismatic plates intersected in the slip plane is rectangular in shape (Ref 17). Nie (Ref 18) reported the effects of prismatic precipitate plates on dispersion strengthening in magnesium alloys based on Orowan strengthening mechanism. Therefore, the contribution of β' phase to yield strength can be estimated by Eq 1 (Ref 18):

$$\sigma_y = \frac{Gb}{2\pi\sqrt{1-\nu} \left(0.825\sqrt{\frac{d_t t_t}{f}} - 0.393d_t - 0.886t_t \right)} \times \ln \frac{0.886\sqrt{d_t t_t}}{b} \quad (\text{Eq 1})$$

where b is the magnitude of the Burgers vector (3.21×10^{-10} m) for Mg (Ref 19); ν is the Poisson's ratio ($\nu = 0.35$); f is the volume fraction; d_t and t_t can be defined by the mean planar diameter $d_p (= \pi d_t/4)$; and the mean planar thickness $t_p (= t_t)$ (Ref 18).

4. Conclusions

Effects of Zn additions and hot-rolling on microstructures and mechanical properties of extruded Mg-6Gd-3.2Y-0.5Zr sheet have been investigated by OM, XRD, SEM, and HRTEM in this article. The investigation leads to the following conclusions:

1. LPSO structures with different forms are found in Mg-6Gd-3.2Y-0.5Zr alloy with Zn addition: the block-shaped ones at grain boundaries and needle-like ones in the interior of the grains. The block-shaped LPSO structures can refine the alloys' microstructures and improve the ability of secondary deformation and improve the tensile mechanical properties of the alloys containing Zn. The needle-like LPSO structures play a beneficial role on the aging-hardening behavior and improve the tensile mechanical properties of the T5 and T10 alloys by decreasing the size of β' phases and making them dispersive.
2. Secondary deformation (extrusion-rolling) can decrease the peak-aging time that increases production efficiency. Secondary deformation can improve the tensile mechanical properties of the T10 alloys by decreasing the size of β' phases and making them dispersive further. The T10 alloy C (1.4 wt.% Zn) obtains the highest proof strength and tensile strength, of 375 and 420 MPa, respectively.

Acknowledgments

This study was supported partly by supported by the National Natural Science Foundation of China (Grant No. 5107486), and the Open-End Fund for the Valuable and Precision Instruments of Central South University. The authors would like to thank Professor Ding Daoyun for providing writing assistance to the article, and the anonymous reviewers for offering the helpful comments.

References

1. S. Schumann and H. Friedrich, Current and Future Use of Magnesium in the Automobile Industry, *Mater. Sci. Forum*, 2003, **419-422**, p 51-56
2. K. Zhang, X.G. LI, and Y.J. LI, Effect of Gd Content on Microstructure and Mechanical Properties of Mg-Y-RE-Zr Alloys, *Trans. Nonferrous Met. Soc. China.*, 2008, **18**, p s12-s16
3. J. Wang, J. Meng, D.P. Zhang, and D.X. Tang, Effect of Y for Enhanced Age Hardening Response and Mechanical Properties of Mg-Gd-Y-Zr Alloys, *Mater. Sci. Eng. A*, 2007, **456**, p 78-84
4. L. Gao, R.S. Chen, and E.H. Han, Fracture Behavior of High Strength Mg-Gd-Y-Zr Magnesium Alloy, *Trans. Nonferrous Met. Soc. China*, 2010, **20**, p 1217-1221
5. S.Q. Liang, D.K. Guan, L. Chen, Z.H. Gao, H.X. Tang, X.T. Tong, and R. Xiao, Precipitation and Its Effect on Age-Hardening Behavior of As-Cast Mg-Gd-Y Alloy, *Mater. Des.*, 2011, **32**, p 361-364
6. Q.M. Peng, Y.M. Wu, D.Q. Fang, J. Meng, and L.M. Wang, Microstructures and Properties of Mg-7Gd Alloy Containing Y, *J. Alloy. Compd.*, 2007, **430**, p 252-256
7. B. Smola, I. Stulikova, F.V. Buch, and B.L. Mordike, Structural Aspects of High Performance Mg Alloys Design, *Mater. Sci. Eng. A*, 2002, **324**, p 113-117
8. T. Honama, T. Ohkubo, K. Hono, and S. Kamado, Chemistry of Nanoscale Precipitates in Mg-2.1Gd-0.6Y-0.2Zr (at.%) Alloy Investigated by the Atom Probe Technique, *Mater. Sci. Eng. A*, 2005, **395**, p 301-306
9. X. Gao, S.M. He, X.Q. Zeng, L.M. Peng, W.J. Ding, and J.F. Nie, Microstructure Evolution in a Mg-15Gd-0.5Zr (wt.%) Alloy During Isothermal Aging at 250°C, *Mater. Sci. Eng. A*, 2006, **431**, p 322-327
10. J.F. Nie, X. Gao, and S.M. Zhu, Enhanced Age Hardening Response and Creep Resistance of Mg-Gd Alloys Containing Zn, *Scr. Mater.*, 2005, **53**, p 1049-1053
11. N. Balasubramani, U.T.S. Pillai, and B.C. Pai, Effect of Zn Concentration on the Microstructure and Phase Formation of Mg-5Gd Alloy, *J. Alloy. Compd.*, 2008, **460**, p L6-L10
12. T. Itoi, T. Seimiya, Y. Kawamura, and M. Hirohashi, Long Period Stacking Structures Observed in Mg97Zn1Y2 Alloy, *Scr. Mater.*, 2004, **51**, p 107-111
13. M. Yamasaki, T. Anan, S. Yoshimoto, and Y. Kawamura, Mechanical Properties of Warm-Extruded Mg-Zn-Gd Alloy with Coherent 14H Long Periodic Stacking Ordered Structure Precipitate, *Scr. Mater.*, 2005, **53**, p 799-803
14. T. Honma, T. Ohkubo, S. Kamado, and K. Hono, Effect of Zn Additions on the Age-Hardening of Mg-2.0Gd-1.2Y-0.2Zr Alloys, *Acta Mater.*, 2007, **55**, p 4137-4150
15. X.L. Hou, Z.Y. Cao, L.L. Zhang, D.Q. Fang, S.W. Xu, S. Kamado, and L.M. Wang, Microstructure and Mechanical Properties of Extruded Mg-6.5Gd-1.3Nd-0.7Y-0.3Zn Alloy, *Trans. Nonferrous Met. Soc. China*, 2010, **20**, p s508-s512
16. L. Ke, L.L. Rokhlin, F.M. Elkin, D.X. Tang, and J. Meng, Microstructures and Mechanical Properties of Extruded Mg-8Gd-0.4Zr Alloys Containing Zn, *Mater. Sci. Eng. A*, 2010, **527**, p 828-834
17. L. Gao, R.S. Chen, and E.H. Han, Microstructure and Strengthening Mechanisms of a Cast Mg-1.48Gd-1.13Y-0.16Zr(at.%) Alloy, *J. Mater. Sci.*, 2009, **44**, p 4443-4454
18. J.F. Nie, Effects of Precipitate Shape and Orientation on Dispersion Strengthening in Magnesium Alloys, *Scr. Mater.*, 2003, **48**, p 1009-1015
19. H.J. Frost and M.F. Ashbv, *Deformation-Mechanism Maps*, Pergamon Press, Oxford, 1982, p 44